Available online at www.sciencedirect.com

SCIENCE DIRECT®

ELSEVIER

Journal of Sound and Vibration 289 (2006) 481–508

JOURNAL OF
SOUND AND
VIBRATION

www.elsevier.com/locate/jsvi

Consideration of piezoceramic actuator nonlinearity in the active isolation of deterministic vibration

Y. Pasco, A. Berry*

G.A.U.S., Mechanical Engineering Department, Université de Sherbrooke, Sherbrooke, Qué., Canada J1K 2R1

Received 15 September 2003; received in revised form 31 January 2005; accepted 13 February 2005
Available online 17 May 2005

Abstract

There is an increasing need to effectively control micro-vibration in such fields as metrology, optics and micro-electronics. This paper describes the design of an adaptive feedforward strategy for vibration isolation of harmonic disturbance using a piezoelectric actuator with hysteretic behavior. A nonlinear analytical model of the piezoelectric actuator including a ferroelectric-like behavior is built using a Preisach model of hysteresis. Pre-multiplication of a single-frequency reference signal by the nonlinear model of the stack is investigated in order to effectively compensate the actuator nonlinearity. It is observed that a simple linear model of the stack is sufficient in the adaptation of a filtered-X LMS feedforward controller to effectively compensate the actuator nonlinearity, provided the reference signal has frequency components at the disturbance frequency and its higher harmonics.

---

1. Introduction

There is an increasing need to effectively control micro-vibration in such fields as metrology, optics and micro-electronics [1]. Traditionally, the control of vibration transmission from a vibratory source to a receiving structure involves passive mounts between the source and receiving structure. However, the performance of passive mounts is usually limited by a trade-off between the required large static stiffness and large dynamic flexibility. A promising alternative in

---

*Corresponding author. Tel.: +1 819 821 8000; fax: +1 819 821 7163.
E-mail addresses: yann.pasco@usherbrooke.ca (Y. Pasco), alain.berry@usherbrooke.ca (A. Berry).

doi:10.1016/j.jsv.2005.02.036

micro-vibration control is the use of active systems based on rigid piezoelectric actuators. Indeed, piezoelectric actuators combine an almost unlimited displacement resolution with a displacement capability in the micrometer range. However, to guarantee a high precision in positioning or in active vibration control applications, nonlinearity of piezoelectric actuators should be taken into account. The nonlinear behavior of piezoelectric actuators originates from an hysteresis between the applied electric field and resulting electric polarization especially under large driving voltage. This translates into significant nonlinearity in the control path and is usually detrimental to the control performance. An approach to address this problem is to linearize the transducer using a control strategy which includes a model of the hysteretic behavior. Previous work has focused on the modeling of a nonlinear transfer function between the electrical input and the mechanical output. Several strategies have been used in recent years like phaser loop feedforward controller [2,3] or Preisach model for hysteresis [4,5]. Adaptive strategies have also been studied such as ARMAX models [6,7], or simple hysteresis operators such as the linear-play operator (LPO) [8–11] in adaptive inverse hysteretic controllers and inverse feedforward controllers. However, these strategies are subject to fail if only the actuator displacement is taken into account in the nonlinear model. A more complete model should include the coupled displacement and force variables of the actuator. The approach introduced here is to use a nonlinear physical model of the actuator as an internal model in an adaptive filtered-X LMS feedforward algorithm. Tiersten [12] contributed significantly to the linear modeling of piezoelectric materials. He also suggested improvements of the linear theory by introducing the electric field dependency of piezoelectric coefficients using higher-order approximations in the case of a large electric field [13]. The use of a mixed variational principle was also used to take into account the recoverable nonlinear behavior of electroelastic materials [14]. In this paper, the physical model is derived from the Huang and Tiersten theory of thermo-electro-elasticity [15], in which the ferroelectric hysteretic behavior is modeled as a discrete mathematical Preisach model of hysteresis [16–18]. This model implies nonrecoverable nonlinearities due to ferroelectric behavior. The physical modeling is applied to a single-axis stack actuator and focuses only on minor loops of hysteresis under operating voltage well-below saturation.

Section 2 presents the nonlinear model of a piezoelectric stack including hysteresis between electric field and polarization that was used in the active control application. Section 3 details the experimental identification of the stack based on a Preisach model of hysteresis. Section 4 presents active control simulations and experiments that were completed using the previous nonlinear model of the control path.

2. A nonlinear model of stack actuators including the electric field versus electric polarization hysteresis

2.1. 3D constitutive equations

The constitutive equations of linear piezoelectricity are the well-known relations [12]

$$\begin{aligned} \sigma_{ij} &= C_{ijkl}\gamma_{kl} - e_{kij}E_k, \\ D_i &= e_{ikl}\gamma_{kl} + \varepsilon_{ik}E_k, \end{aligned} \qquad (1)$$

where σ, γ, E, D denote the stress tensor, strain tensor, electric field and electric displacement, respectively; C, e and ε are the usual elastic, piezoelectric and dielectric susceptibility tensors. Piezoelectric stack actuators generally do not conform to Eq. (1) because of ferroelectric hysteresis: the dipole orientation (and therefore electric polarization or electric displacement) of the piezoelectric medium does not follow instantly the changes of the electric field, giving rise to hysteresis. Huang and Tiersten have suggested an analytical framework for polarized piezoceramics under ferroelectric hysteresis and have investigated the case of piezoelectric plates with a polynomial approximation of hysteresis [15]. In this theory, the electric polarization $\mathbf{P} = \varepsilon_0\mathbf{E} - \mathbf{D}$ (ε_0 is the void electric permittivity) of the piezoelectric continuum is broken in a part $\tilde{\mathbf{P}}$ linearly related to $\mathbf{E}$, and a nonlinear part $\hat{\mathbf{P}}$ which is the image of the ferroelectric nonlinearity,

$$\mathbf{P} = \tilde{\mathbf{P}} + \hat{\mathbf{P}}. \tag{2}$$

The general constitutive equations of piezoelectricity have been obtained by Huang and Tiersten under small displacement assumption and hysteresis along one-axis only [15]. These equations have recently been generalized by Pasco for an arbitrary direction of polarization [16,17]. The following new thermodynamical functional accounting for electric hysteresis, material anisotropy and small mechanical was proposed

$$\begin{aligned}\rho_0\chi = {} & \tfrac{1}{2}C_{ijkl}\gamma_{ij}\gamma_{kl} - e_{kij}E_k\gamma_{ij} - \tfrac{1}{2}\varepsilon_{ij}E_iE_j + \tfrac{1}{2}\rho_0 d_{mijkl}\hat{\Pi}_m\gamma_{ij}\gamma_{kl} \\ & - \rho_0 g_{klij}\hat{\Pi}_k E_l\gamma_{ij} - \tfrac{1}{2}\rho_0 a_{kij}\hat{\Pi}_k E_iE_j - \rho_0\alpha_{kij}\hat{\Pi}_k\gamma_{ij} - \rho_0\hat{\Pi}^0_i E_i,\end{aligned} \tag{3}$$

where $\hat{\Pi} = \hat{P}/\rho_0$ is the specific electric polarization, ρ_0 is the mass density of the medium, d, g, a, α are tensors of ferro-electro-elastic interaction coefficients first introduced by Tiersten and $\hat{\Pi}^0_i$ is the initial remanent specific polarization in each direction i. Assuming an anisotropic material, the constitutive equations associated to the thermodynamical functional equation (3) are, in contracted form [16,17]:

$$\begin{aligned}P_i &= e_{i\alpha}\gamma_\alpha + \varepsilon_{ij}E_j + g_{ji\alpha}\hat{P}_j\gamma_\alpha + a_{kij}\hat{P}_kE_j + \hat{P}^0_i + \hat{P}_i, \\ \sigma_\alpha &= C_{\alpha\beta}\gamma_\beta - e_{i\alpha}E_i + d_{i\alpha\beta}\hat{P}_i\gamma_\beta - g_{ij\alpha}\hat{P}_iE_j - \alpha_{i\alpha}\hat{P}_i.\end{aligned} \tag{4}$$

In Eq. (4), the first 2 terms on the right-hand side of the equality account for linear piezoelectricity. The remaining terms are used to correct coefficients in the linear terms as a result of the irreversible polarization, as well as introduce a constitutive dependence on the irreversible polarization itself. In this formulation, nonlinearities are introduced by the hysteresis effect between polarization $\hat{P}$ and the electric field E, $\hat{P}^0_i$ is the initial remanent polarization in each direction i and d, g, a, α are tensors of ferro-electro-elastic interaction coefficients first introduced by Tiersten. These additional coefficients eventually need to be identified by experiments. Note that an alternative form of Eq. (4) is

$$\begin{aligned}P_i &= (e_{i\alpha} + g_{ji\alpha}\hat{P}_j)\gamma_\alpha + (\varepsilon_{ij} + a_{kij}\hat{P}_k)E_j + \hat{P}^0_i + \hat{P}_i, \\ \sigma_\alpha &= (C_{\alpha\beta} + d_{i\alpha\beta}\hat{P}_i)\gamma_\beta - (e_{i\alpha} + g_{ji\alpha}\hat{P}_j)E_i - \alpha_{i\alpha}\hat{P}_i.\end{aligned} \tag{5}$$

By comparing Eqs. (1) and (5), it is clear that the nonlinearity effectively modifies the classical elastic, piezoelectric and dielectric coefficients of the medium.

2.2. Reduction to a stack actuator

The general, 3D constitutive equations (4) are applied to a piezoelectric stack actuator with electrodes in parallel configuration (Fig. 1). Stack actuators are made of several thin layers of piezoelectric material subject to an electric field in the thickness direction (defined in the direction 3), and are used to generate motion or forces also in the thickness direction. The lateral surfaces consequently have free mechanical and electrical boundary conditions. Electrodes and bonding layers were assumed to be thin enough to ensure continuity of the axial stress gradient of the entire body of the actuator. Therefore, the actuator can be assumed to be geometrically identical to a uniaxial rod. Since the electric field is applied in a layer's thickness direction, and this thickness is small compared to its lateral dimension, it is appropriate to consider the electric field in a layer independent of the lateral dimensions (1 and 2). Because of the continuity of the electric displacement and the free electrical and mechanical boundary conditions in the transverse directions, the electric polarization in the lateral directions must vanish. As a consequence, the nonlinear part of the electric polarization will exist only in the axis of the actuator

$$E_i = \delta_{i3} E_3,$$

$$\hat{P}_i = \delta_{i3} \hat{P}_3, \tag{6}$$

where δ_{ij} is the Kronecker-delta symbol. The total axial displacement of the actuator is given by

$$\delta l_{\text{total}} = \int_H \gamma_3 \, \mathrm{d}l = n \int_h \gamma_3 \, \mathrm{d}h, \tag{7}$$

where n is the number of layers and h is their thickness. Therefore, the behavior of the whole actuator can be derived from the behavior of a single layer. The stress in the stack is uniaxial, so that $\sigma_3 = f$ and $\sigma_i = 0$, $i \neq 3$, where f is the axial stress applied to the stack (Fig. 2). In the case of quasi-static mechanical displacement (far below the first natural frequency of the actuator), forces

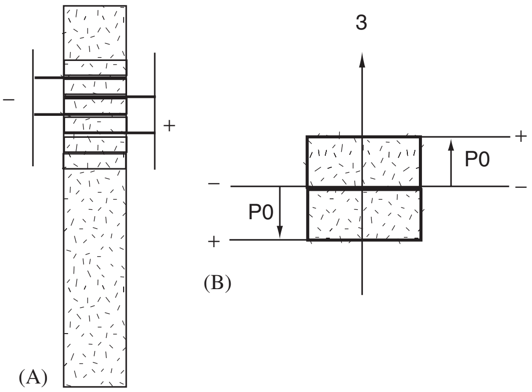

Fig. 1. Geometrical configuration of a stack actuator showing the positive and negative terminals and the direction of initial polarization P_0.

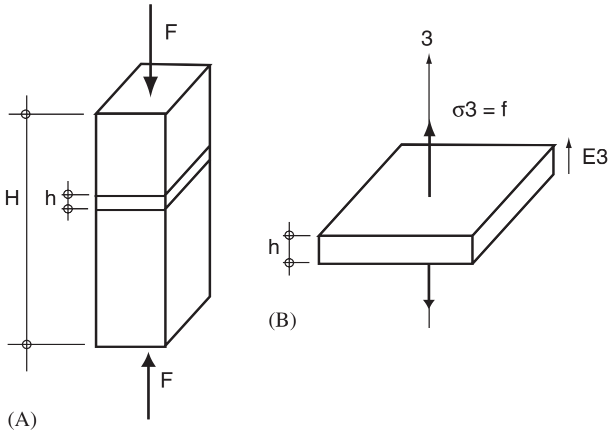

Fig. 2. Uniaxial load F applied to the stack actuator (total thickness H) and resulting pressure ($\sigma_3 = f$) applied on each layer (thickness h).

due to inertia are neglected. Applying these assumptions and Eq. (6) to the constitutive equations (4) results in the following constitutive nonlinear equations of a stack actuator:

$$\sigma_3 = \frac{A_{\sigma\gamma}\hat{P}_3^2 + B_{\sigma\gamma}\hat{P}_3 + C_{\sigma\gamma}}{A\hat{P}_3 + B}\gamma_3 + \frac{A_{\sigma E}\hat{P}_3^2 + B_{\sigma E}\hat{P}_3 + C_{\sigma E}}{A\hat{P}_3 + B}E_3 + \frac{A_{\sigma}\hat{P}_3^2 + B_{\sigma}\hat{P}_3}{A\hat{P}_3 + B},$$

$$P_3 = \frac{A_{P\gamma}\hat{P}_3^2 + B_{P\gamma}\hat{P}_3 + C_{P\gamma}}{A\hat{P}_3 + B}\gamma_3 + \frac{A_{PE}\hat{P}_3^2 + B_{PE}\hat{P}_3 + C_{PE}}{A\hat{P}_3 + B}E_3 + \frac{A_{P}\hat{P}_3^2 + B_{P}\hat{P}_3}{A\hat{P}_3 + B} + \hat{P}_3^0,$$

$$P_1 = P_2 = 0,$$

$$E_1 = E_2 = 0 \tag{8}$$

and

$$\gamma_1 = \gamma_2 = \frac{(-\hat{P}_3 d_{313} - c_{13})\gamma_{33} + (e_{331} + \hat{P}_3 g_{331})E_3 + \hat{P}_3\alpha_{31}}{A\hat{P}_3 + B}, \tag{9}$$

where the various constants that appear in Eqs. (8) and (9) depend on the usual elastic, piezoelectric, dielectric coefficients and the new ferro-electro-elastic coefficients,

$$A = d_{311} + d_{312},$$

$$B = c_{11} + c_{12},$$

$$A_{\sigma\gamma} = d_{333}(d_{311} + d_{312}) - 2d_{313}^2,$$

$$B_{\sigma\gamma} = c_{33}(d_{311} + d_{312}) + (c_{11} + c_{12})d_{333} - 4c_{13}d_{313},$$

$$C_{\sigma\gamma} = (c_{11} + c_{12})c_{33} - 2c_{13}^2,$$

$$A_{\sigma E} = -A_{P\gamma} = -g_{333}(d_{311} + d_{312}) + 2d_{313}g_{331},$$

$$B_{\sigma E} = -B_{P\gamma} = -e_{33}(d_{311} + d_{312}) - (c_{11} + c_{12})g_{333} + 2c_{13}g_{331} + 2d_{313}e_{31},$$

$$C_{\sigma E} = -C_{P\gamma} = -(c_{11} + c_{12})e_{33} + 2c_{13}e_{31},$$

$$A_{\sigma} = 2d_{313}\alpha_{31} - (d_{311} + d_{312})\alpha_{33},$$

$$B_{\sigma} = 2c_{13}\alpha_{31} - (c_{11} + c_{12})\alpha_{33},$$

$$A_{PE} = a_{333}(d_{311} + d_{312}) + 2g_{331}^2,$$

$$B_{PE} = \varepsilon_{33}(d_{311} + d_{312}) + (c_{11} + c_{12})a_{333} + 4e_{13}g_{331},$$

$$C_{PE} = (c_{11} + c_{12})\varepsilon_{33} - 2e_{31}^2,$$

$$A_P = 2g_{331}\alpha_{31} + d_{311} + d_{312},$$

$$B_P = 2e_{31}\alpha_{31} + c_{11} + c_{12}. \tag{10}$$

Eqs. (8)–(10) show that the nonlinear model of the stack actuator depends on the irreversible polarization $\hat{P}_3$ and on the ferro-electro-elastic coefficients d_{311}, d_{312}, d_{313}, d_{333}, g_{331}, g_{333}, α_{31}, α_{33}. As a comparison the linear equations of the stack actuator ($\hat{P}_3 = 0$) would simplify to

$$\sigma_3 = \frac{C_{\sigma\gamma}}{B}\gamma_3 + \frac{C_{\sigma E}}{B}E_3,$$

$$P_3 = \frac{C_{P\gamma}}{B}\gamma_3 + \frac{C_{PE}}{B}E_3. \tag{11}$$

In order to implement the nonlinear model of the stack described by Eq. (8), it is necessary to determine both the nonlinear part of the polarization $\hat{P}_3$ and the ferro-electro-elastic coefficients

d_{311}, d_{312}, d_{313}, d_{333}, g_{331}, g_{333}, α_{31}, α_{33} that appear in Eq. (10). In the following, an experimental procedure is presented to identify both $\hat{P}_3$ and the ferro-electro-elastic coefficients. The nonlinear part of the polarization $\hat{P}_3$ is identified using a Preisach model of hysteresis and the ferro-electro-elastic coefficients are identified using a least-squares fit from the experimental data. It is assumed here that the usual elastic, piezoelectric and dielectric constants c, e and ε of the material are known a priori.

3. Experimental identification of a piezoelectric stack actuator

3.1. Preisach model of ferroelectric hysteresis

This section is concerned with the identification of the irreversible polarization $\hat{P}_3$ in the nonlinear constitutive equations of the stack. The modeling of hysteresis in ferroelectric materials is discussed in Ref. [16]. In this paper, the polarization versus electric field hysteresis of a piezoceramic material is modeled with a Preisach model. The governing equation for the Preisach model of hysteresis is [18]

$$P_{\mathrm{Pr},3}(t) = \int\int_{\mathscr{P}} \mu(\alpha,\beta)[\hat{\Gamma}_{\alpha\beta}E_3](t)\,\mathrm{d}\alpha\,\mathrm{d}\beta. \tag{12}$$

The hysteretic operator $\hat{\Gamma}_{\alpha\beta}$ is called a Hysteron and can be interpreted as an elementary relay hysteresis (see Fig. 3). The pair (α,β) with $\alpha \geqslant \beta$ define switching values for which the output of the hysteron $\hat{\Gamma}_{\alpha\beta}$ changes its value; the variables α, β take their values between the minimum and maximum values of the applied electric field, $E_{\min}$ and $E_{\max}$. The output of the hysteron $\hat{\Gamma}_{\alpha\beta}$ can take only two values: -1 or $+1$. The domain $\mathscr{P}$ is defined as the half-plane $\mathscr{P} = \{(\alpha,\beta) \mid \alpha \geqslant \beta\}$; a pair of values (α,β) thus defines a given hysteron, and a continuum of hysterons have to be considered in order to build the model. At any given time, the domain $\mathscr{P}$ is divided into two sub-domains $\mathscr{P}_-$ and $\mathscr{P}_+$ which are defined as the set of (α,β) values for which $\hat{\Gamma}_{\alpha\beta} = -1$ and $\hat{\Gamma}_{\alpha\beta} = +1$, respectively. The surface $\mu(\alpha,\beta)$ defines weights of elementary hysterons in the calculation of the output $P_{\mathrm{Pr}}(t)$.

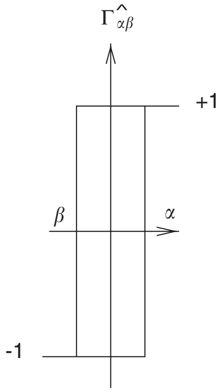

Fig. 3. Hysteron $\hat{\Gamma}_{\alpha\beta}$ of an elementary domain and unpolarized state in a general Preisach model of hysteresis.

The constitutive equations (8) show that the new ferro-electro-elastic constants are defined from the nonlinear part of the polarization $\hat{\mathbf{P}}$ only. Therefore, the value of $\hat{\mathbf{P}}$ must only take in to account the nonlinear contribution of the model [15],

$$\hat{P}_3 = P_{\mathrm{Pr},3}(E_3) - \beta E_3. \tag{13}$$

It can be shown [15–17] that the linear rate β is related to the piezoelectric coefficients e_{31}, e_{33} and the new coefficients α_{31} and α_{33} by

$$\beta = \frac{e_{31}}{\alpha_{31}} = \frac{e_{33}}{\alpha_{33}}. \tag{14}$$

Therefore, the values of two of the new ferro-electro-elastic constants α_{31} and α_{33} are known provided β is known.

3.2. Experimental setup and identification

A BM532 PZT5H piezoceramic actuator (provided by Sensor Technology Limited) was used in the experiments. It consists of a 50 layers stack, each layer having a 0.2 mm thickness. The maximal-free displacement is about 3 μm for an applied voltage of 100 V in the 33 direction, and the useful force generated is about 150 N (for a displacement capability of 25% of the maximal free displacement). In the experiments, one end of the stack was fixed and the other end was free (corresponding to $\sigma_3 = 0$ in Eq. (8)). A depolarization electrical cycle was also applied on the actuator before identification of the new constants. It consists of a large amplitude, periodic electric field decreasing to zero in amplitude to achieve a zero dynamic polarization initial state. This was used to make sure that the initial static polarization state is the same for each experiment.

As detailed previously, the identification of the new model of the stack consists of two independent optimizations: first, the Preisach model for the nonlinear relation between electric field and polarization is identified according to Eq. (12), in order to obtain the irreversible part $\hat{P}_3$; second, the new ferro-electro-elastic coefficients of the stack are derived from Eqs. (8) and (10). The identification requires measuring the free displacement of the stack, applied voltage and polarization. The free displacement d and applied voltage U are related to the transverse deformation and electric field through $d = nh\gamma_3$, $U = -hE_3$ where n is the number of layers in the stack and h is the thickness of a layer. The free displacement at the top of the stack actuator was derived from the velocity measured using a Doppler laser vibrometer. The average electric polarization was measured using a Sawyer–Tower bridge: by measuring the voltage U_0 between the two electrodes of a known serial capacitance c_0, one can obtain the average electric polarization of the stack electrodes using the relation

$$P_3 = \frac{U_0 c_0}{nS} - \varepsilon_0 \frac{U - U_0}{h},$$

where S is the area of the stack electrode [17].

All these signals (transverse velocity at stack's free end, applied voltage and average polarization of stack electrodes) were measured synchronously using a 32 input/output real-time Dspace system. In this article, experimental hysteresis cycles are plotted on an average time period (where the cycle is stable), and cycles identified from the model are plotted assuming an initial state of zero polarization, since the initial spontaneous polarization cannot be identified using the Sawyer–Tower circuit.

3.2.1. Identification of the polarization

In theory, the saturation curve of the piezoceramic is necessary to construct the Preisach model of major hysteresis loops [19]. However, in the case of a stack actuator, the large electric field necessary to obtain a saturation of the ceramic is not easily reached. This study rather focused on the measurement and identification of minor hysteresis loops (Fig. 4). As discussed previously, the initial spontaneous polarization P_3^0 was not measured in the experiments and was assumed to be zero in the model. The Preisach mathematical model of minor loops was built with the method described by Mayergoyz [18]. In order to determine $\mu(\alpha, \beta)$, a set of first-order reversal curves of hysteresis is needed. Experimentally, these curves can be obtained by first decreasing the applied voltage to the smallest needed to bring all hysterons to the -1 state. Next, the voltage is monotonically increased to a value α (this curve corresponds to an ascending branch of the minor loop) and finally, the applied voltage is decreased to a new fixed value β. The measured polarization of the stack corresponding to the conditions α and β is noted $f_{\alpha\beta}$ (Fig. 5). This operation needs to be repeated to cover all values of α and β in the interval of the operating

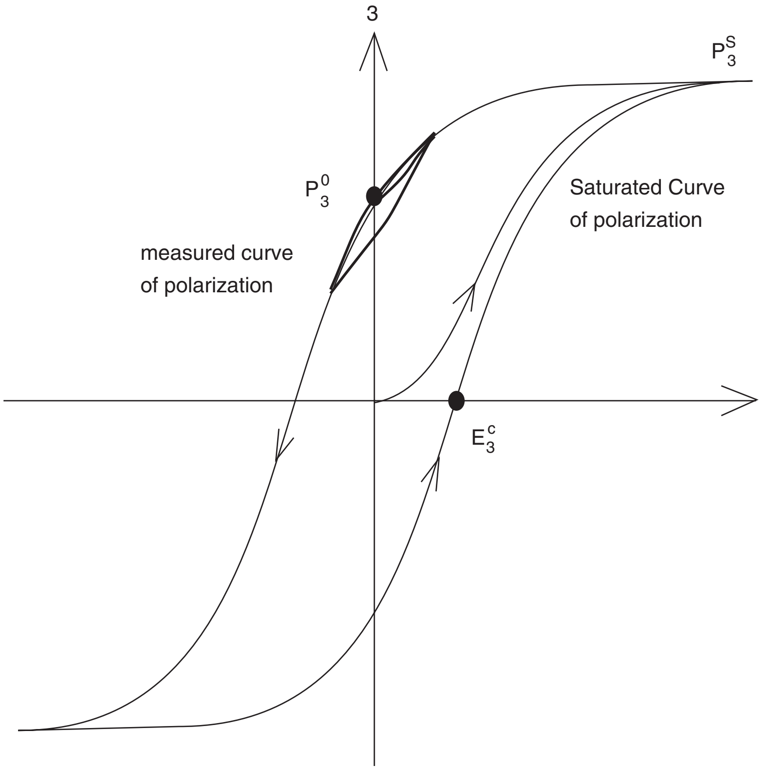

Fig. 4. Saturation curve of polarization (thin) and measured curve (bold) for an increasing and decreasing applied voltage (initial polarization P_3^0, saturation polarization P_3^s and coercitive electric field E_3^0).

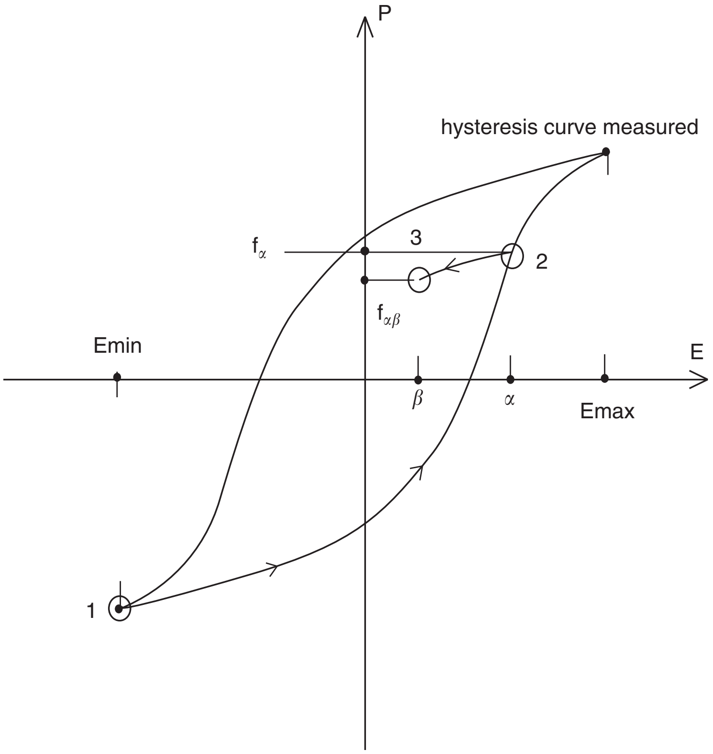

Fig. 5. Measuring reversal curves of polarization P as a function of the electric field E: methodology to obtain the coefficients $f_{\alpha\beta}$ of the Preisach ponderation surface.

applied voltage, and the resulting polarization $f_{\alpha\beta}$ is measured for each combination of α and β. In our case the applied voltage varied between $U_{\min} = -100\,\text{V}$ and $U_{\max} = 100\,\text{V}$ (corresponding to an applied electric field between $E_{\min} = -2.5 \times 10^5\,\text{V/m}$ and $E_{\max} = 2.5 \times 10^5\,\text{V/m}$ in each layer).

According to Mayergoyz [18], the weighting surface μ in Eq. (12) is related to the measured polarization $f_{\alpha\beta}$ by the relation

$$\mu(\alpha, \beta) = \frac{1}{2}\frac{\partial^2 f_{\alpha\beta}}{\partial\alpha\partial\beta}.$$

The determination of μ therefore involves finite double differentiation of the measured polarization. However, results obtained by finite differentiation are accurate only if the number of points is large. In order to compute the weights, it was chosen instead to use a simple parameterization of the weighting surface $\mu(\alpha, \beta)$ borrowed from ferromagnetic hysteresis modeling [20]. In this model, the (α, β) plane is mapped to the (E_i, E_c) plane, where E_i and E_c are two new variables in $[E_{\min}, E_{\max}]$ defined by $\alpha = E_i + E_c$ and $\beta = E_i - E_c$.

The parameterized weighting surface is defined in $[E_{\min}, E_{\max}]$ by

$$\mu_{(\alpha\geqslant\beta)} = P_{\max}[(1-c)\mu_{\alpha>\beta} + c\mu_{(\alpha=\beta)}], \tag{15}$$

where

$$\mu_{(\alpha=\beta)} = \frac{1 + \left[\dfrac{E_i X_a}{2P_{\max}/\pi}\right]^2}{\int_{E_{\min}}^{E_{\max}} \left(1 + \left[\dfrac{E X_a}{2P_{\max}/\pi}\right]^2\right) \mathrm{d}E},$$

$$\mu_{(\alpha>\beta)} = \frac{\mathrm{e}^{-((E_c - E_0)/E_0)^2}}{1 + \left[\dfrac{E_i X_a}{2P_{\max}/\pi}\right]^2} \tag{16}$$

and $\{P_{\max} X_a E_0 c\}^{\mathrm{T}}$ is the vector of the parameters to be identified in the model. These parameters represent, respectively, the maximum electric polarization reached in the range of applied electric field, the initial rate of polarization, the remanent electric field and finally, a weighting coefficient which is used when the polarization saturation is not reached in the range of applied electric field. The coefficient c can be reduced to zero to model a complete saturation curve.

The identification of these parameters relies on a method of unconstrained minimization that minimizes the squared norm of the vector containing the differences between an evaluation of the model versus the experimental data. The electric polarization calculated from the model and experimentally measured as a function of electric field, are the only data needed to compute the optimization. The method uses the algorithm of Levenberg–Marquardt [21,22]. During the experiments, the applied electric field $E(t) = E_3(t)$ was chosen as a sinusoidal signal on a single period to achieve identification by the use of the Sawyer–Tower bridge. The frequency of the signal should normally ensure that the quasi-static electric field hypothesis is satisfied. A frequency of 150 Hz was chosen. It is important to note that since quasi-static identification is not allowed by the use of the Sawyer–Tower bridge, the identified parameters are related to minor hysteresis loops around the initial state of polarization. The sampling rate was 9000 Hz, therefore 60 points were obtained per stable cycle. After running the minimization algorithm, the optimized values of the model parameters found are $\{P_{\max} X_a E_0 c\}^{\mathrm{T}} = \{0.063\,\mathrm{C/m^3}; 1.558 \times 10^{-8}\,\mathrm{C/V\,m^2}; 2.877 \times 10^4\,\mathrm{V/m}; 0.645\}^{\mathrm{T}}$. The value found for c is not zero which confirms that the electric field used is far from saturation. The above values were used to construct the weighting surface according to Eq. (15). A discrete version of the Preisach model, Eq. (12) was then implemented using a 51×51 matrix of values $\mu(\alpha_i, \beta_j)$ defined for regularly spaced values α_i and β_j in the operating range of electric field.

3.2.2. *Identification of the new ferro-electro-elastic coefficients*

The vector of the new ferro-electro-elastic constants

$$\{d_{311}\ d_{312}\ d_{313}\ d_{333}\ g_{331}\ g_{333}\ \beta\}^{\mathrm{T}}$$

is identified using the experimental data of displacement, applied electric field and polarization of the stack, together with Eqs. (8), (13) and the identified Preisach model between polarization and electric field. The same Levenberg–Marquardt optimization method is used to derive optimal values of the constants such that the deviation between Eq. (8) and the experimental data is minimized. A sinusoidal voltage was applied to the stack between $U_{\min} = -100\,\mathrm{V}$ and $U_{\max} = 100\,\mathrm{V}$, and the frequency used for the identification was 150 Hz.

The usual linear constants of the stack used in the model are those for PZT5H: for this material, the compliance matrix is

$$[s] = 1 \times 10^{-12} \begin{bmatrix} 16.5 & -4.78 & -8.45 & 0 & 0 & 0 \\ -4.78 & 16.5 & -8.45 & 0 & 0 & 0 \\ -8.45 & -8.45 & 20.7 & 0 & 0 & 0 \\ 0 & 0 & 0 & 43.5 & 0 & 0 \\ 0 & 0 & 0 & 0 & 43.5 & 0 \\ 0 & 0 & 0 & 0 & 0 & 42.6 \end{bmatrix}. \tag{17}$$

The piezoelectric strain constant matrix is

$$[d] = 1 \times 10^{-12} \begin{bmatrix} 0 & 0 & 0 & 0 & 741 & 0 \\ 0 & 0 & 0 & 741 & 0 & 0 \\ -274 & 593 & 0 & 0 & 0 & 0 \end{bmatrix}. \tag{18}$$

The permittivity constant matrix is

$$[\varepsilon] = 8.854 \times 10^{-12} \begin{bmatrix} 3130 & 0 & 0 \\ 0 & 3130 & 0 \\ 0 & 0 & 3400 \end{bmatrix}. \tag{19}$$

Therefore, the elastic constants $[c]$ and piezoelectric charge constants $[e]$ which are used in the model are given by $[c] = [s]^{-1}$ and $[e] = d[s]^{-1}$. The identified new ferro-electro-elastic coefficients found after minimization are

$$d_{311} = -4.96 \times 10^{12}\,\mathrm{N/C},$$

$$d_{312} = -3.82 \times 10^{12}\,\mathrm{N/C},$$

$$d_{313} = -3.82 \times 10^{12}\,\mathrm{N/C},$$

$$d_{333} = -1.99 \times 10^{12}\,\mathrm{N/C},$$

$$g_{331} = 1.45 \times 10^{5}\,\mathrm{N\,V/C\,m},$$

$$g_{333} = 1.13 \times 10^{5}\,\mathrm{N\,V/C\,m},$$

$$\alpha_{31} = -2.25 \times 10^{8}\,\mathrm{N/C},$$

$$\alpha_{33} = 7.90 \times 10^{8}\,\mathrm{N/C},$$

$$\beta = 2.94 \times 10^{8}\,\mathrm{C/V\,m}.$$

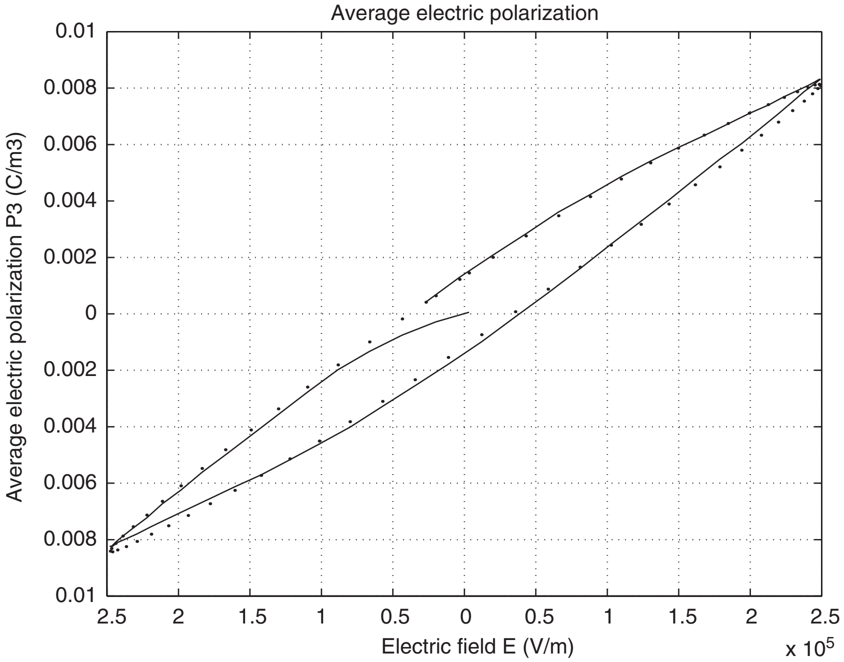

Fig. 6. Polarization P_3 versus applied electric field E_3, hysteresis of the BM532 PZT5H piezoceramic actuator (measurement: dotted line, model using the Preisach operator: solid line).

These constants are to be compared with the ones estimated by Huang et al. for plates [15]. As an example, these authors identified the two first plate constants $d_1^p = -4.3 \times 10^{12}\,\mathrm{N/C}$ and $d_2^p = -2.2 \times 10^{12}\,\mathrm{N/C}$. These values are comparable to our values of d_{311} and d_{312}.

Fig. 6 shows the measured hysteresis between electric field and polarization as well as the Preisach model identification. The Preisach model is in good agreement with the measured data. Fig. 7 shows the measured hysteresis between electric field and generated displacement on top of the stack, together with the model identification; again, the model appropriately describes the hysteresis in terms of mechanical displacement versus applied electric field. Fig. 8 presents the measured free displacement of the stack versus time, as well as linear and nonlinear model results (in the linear case, only the linear constants were used in the model, according to Eq. (11)). These results clearly show that the linear model significantly deviates from the measured data; on the other hand, the nonlinear model dramatically improves the prediction in terms of generated displacement. The following section investigates the use of the nonlinear model of the stack actuator in active vibration isolation experiments.

4. Active vibration isolation using a piezoelectric stack actuator: Analysis and simulations

The application presented in this section involves the isolation of deterministic (single frequency) vibrations from a vibrating base to a platform, representing e.g. a sensitive equipment

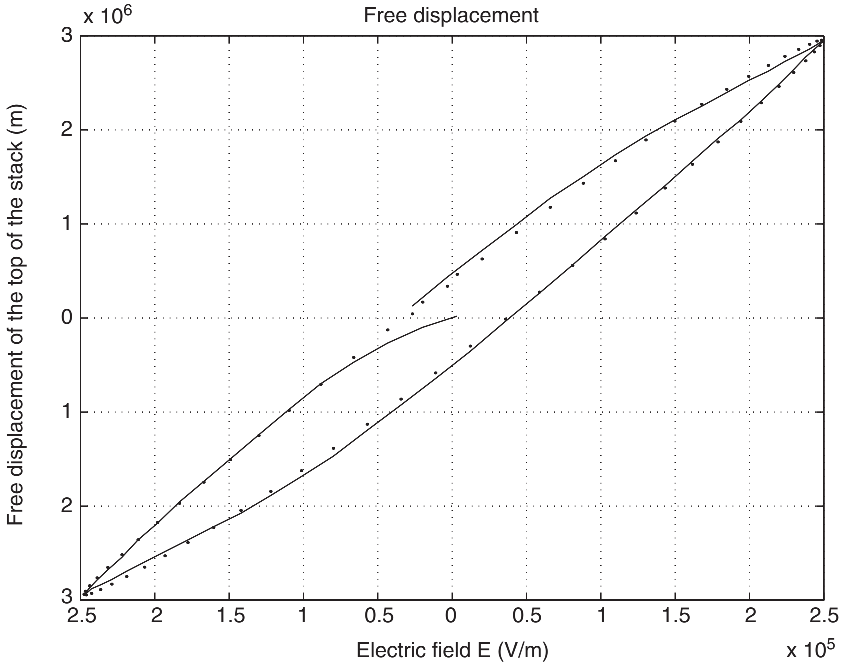

Fig. 7. Displacement δl_{total} versus electric field E_3 hysteresis of the BM532 PZT5H piezoceramic actuator (measurement: dotted line, model using the Preisach operator: solid line).

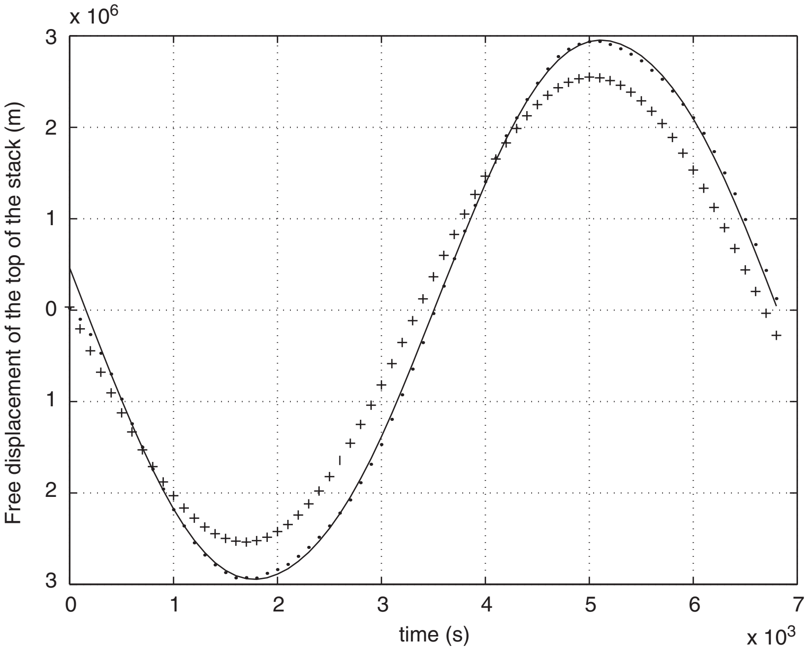

Fig. 8. Displacement δl_{total} versus time of the BM532 PZT5H piezoceramic actuator: linear ("+" line) and nonlinear (dotted line) identification and measurement (solid line).

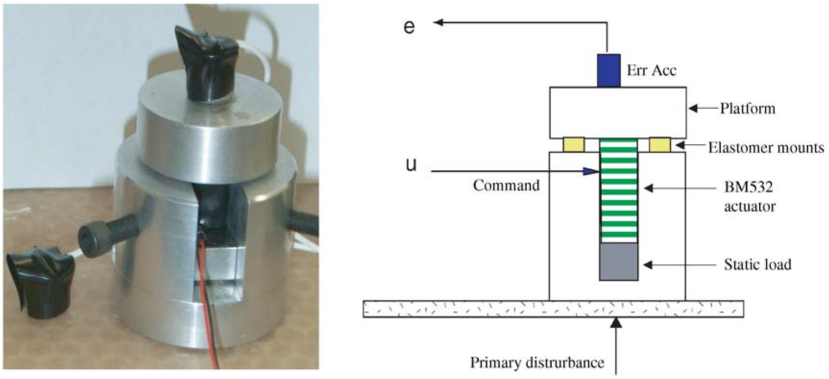

Fig. 9. Schematics and photograph of the tested active isolator. u, e are, respectively, the applied voltage and the error signal.

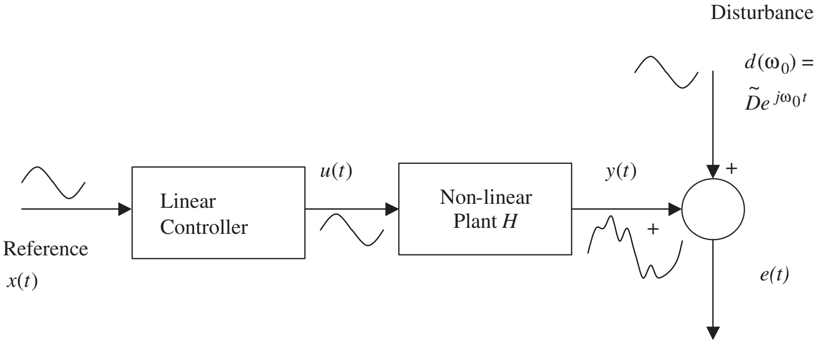

Fig. 10. Feedforward control of a harmonic disturbance d with a nonlinear plant.

to be isolated from ground vibrations. A one-axis active isolator was implemented with one stack actuator to control the transmission of vibration in the transverse direction only, Fig. 9. A reference signal of the base excitation is used in an adaptive feedforward controller to cancel the acceleration transmitted to the platform. In general, the propagation delay of the disturbance between the reference sensor and the top of the stack is smaller than the iterative turnaround controller time, so that causality would not be respected for random base perturbation [3]; however, only the case of deterministic perturbation is considered here, and causality is therefore not a constraint. Fig. 10 shows the corresponding general feedforward control situation. In this figure, x is the reference signal, $d(\omega_0) = \tilde{D}e^{j\omega_0 t}$ is the single-frequency disturbance and H denotes the plant, or control path (between the control signal u and the signal e provided by an error accelerometer mounted on the platform). The previous sections have shown that H is a nonlinear path. In the following, it is assumed that the piezoelectric stack is a *weakly* nonlinear actuator, in the sense that the actuator output y to a single-frequency input u at ω_0 is completely described in steady state by frequency components at ω_0 and at multiples $n\omega_0$ with amplitudes well bellow the fundamental. This is justified by the fact that the actuator operates far below saturation and as a consequence, the hysteresis is due to a minor loop of ferro-electric polarization. Therefore, in the case of a single-frequency disturbance and a perfectly linear controller, the nonlinear behavior of the stack actuator results in harmonic generation on the suspended mass, which in general degrades the control performance. In the following sections, a time-domain adaptive feedforward control architecture is investigated to compensate for the actuator nonlinearity.

4.1. Frequency-domain analysis

The problem of rejecting a harmonic disturbance $d(\omega_0) = \tilde{D}\exp(\mathrm{j}\omega_0 t)$ using a feedforward controller and a nonlinear plant is shown in Fig. 10. Note that in this case, the reference signal is a harmonic signal at the fundamental frequency ω_0, $x(t) = x(\omega_0) = \mathrm{e}^{\mathrm{j}\omega_0 t}$. Therefore, it is anticipated that higher harmonics of the fundamental frequency generated by the nonlinear plant will be present in the error signal. Although Fig. 10 assumes that the plant output and disturbance linearly add, in reality the disturbance will in general modify the operating point of the actuator and therefore modify its response [3]. However, the assumption that the plant output and disturbance linearly add simplifies the analysis.

In the following, we address the problem of adjusting the complex gain of the controller $\tilde{\Gamma}(\omega_0)$ in order to minimize the error signal $e(t)$. According to the previous assumption concerning the plant, the plant output can be written as a linear superposition of harmonic signals,

$$y(t) = \sum_{n=0}^{N} \tilde{y}_n \mathrm{e}^{\mathrm{j}n\omega_0 t}. \tag{20}$$

Note that in the previous equation, $n = 0$ defines the DC output and therefore the operating point of the nonlinear plant. The error signal is

$$e(t) = \sum_{n=0}^{N} \tilde{y}_n \mathrm{e}^{\mathrm{j}n\omega_0 t} + \tilde{D}\mathrm{e}^{\mathrm{j}\omega_0 t}. \tag{21}$$

We define the criterion to be the energy of the error signal averaged over one fundamental period,

$$J = \frac{1}{T_0}\int_0^{T_0} [\mathrm{Re}(e(t))]^2 \,\mathrm{d}t. \tag{22}$$

After some algebra and using the Parseval theorem, we obtain

$$J = \frac{1}{2}\sum_{n \neq 1} |\tilde{y}_n|^2 + \frac{1}{2}|\tilde{y}_1 + \tilde{D}|^2 = \frac{1}{2}\mathbf{e}^H\mathbf{e}, \tag{23}$$

where $\mathbf{e} = [\tilde{y}_0 \tilde{y}_1 + \tilde{D} \tilde{y}_2 \ldots \tilde{y}_N]^{\mathrm{T}}$. On the other hand, the control input is given by $u(\omega_0) = \tilde{\Gamma}(\omega_0)\mathrm{e}^{\mathrm{j}\omega_0 t}$. In general, J is not a quadratic function of the complex control gain $\tilde{\Gamma}(\omega_0)$, because there may exist a nonlinear relation between the harmonic components of the error signal and the complex control gain. However, the simplest adaptation algorithm is to iteratively adjust this control gain in the direction opposite to the gradient $\partial J/\partial\tilde{\Gamma}$.

$$\frac{\partial J}{\partial \tilde{\Gamma}} = \frac{\partial(\frac{1}{2}\mathbf{e}^H\mathbf{e})}{\partial \tilde{\Gamma}} = \frac{\partial \mathbf{e}^H}{\partial \tilde{\Gamma}}\mathbf{e} = \frac{\partial \mathbf{y}^H}{\partial \tilde{\Gamma}}\mathbf{e}, \tag{24}$$

where $\mathbf{y} = [\tilde{y}_0\ \tilde{y}_1\ \tilde{y}_2 \ldots \tilde{y}_N]^{\mathrm{T}}$. The steepest-descent algorithm writes

$$\tilde{\Gamma}(n+1,\omega_0) = \tilde{\Gamma}(n,\omega_0) - \mu \frac{\partial J}{\partial \tilde{\Gamma}(n,\omega_0)} \tag{25}$$

$$= \tilde{\Gamma}(n,\omega_0) - \mu \left[\frac{\partial \tilde{y}_0^*}{\partial \tilde{\Gamma}}\ \frac{\partial \tilde{y}_1^*}{\partial \tilde{\Gamma}}\ \cdots\ \frac{\partial \tilde{y}_N^*}{\partial \tilde{\Gamma}} \right] \mathbf{e}, \tag{26}$$

where μ is the adaptation coefficient and * denotes the complex conjugate. The vector

$$\left[\frac{\partial \tilde{y}_0^*}{\partial \tilde{\Gamma}}\ \frac{\partial \tilde{y}_1^*}{\partial \tilde{\Gamma}}\ \cdots\ \frac{\partial \tilde{y}_N^*}{\partial \tilde{\Gamma}} \right]$$

is equivalent to the sensitivity matrix introduced by Elliott [3,23] and represents the sensitivity of the harmonics generated by the control actuator with respect to the actuator input at the fundamental frequency ω_0. This matrix will in general depend of the operating point of the actuator, and needs to be identified. The above equation shows that for a nonlinear control actuator, the update of the controller gain takes into account the generation of higher harmonics by the actuator. Since there are $N+1$ complex harmonic amplitudes to be controlled and only one complex control gain, it is not possible to independently control all harmonics with the structure shown in Fig. 10.

Note that if the plant is perfectly linear, the update equation becomes

$$\tilde{\Gamma}(n+1,\omega_0) = \tilde{\Gamma}(n,\omega_0) - \mu \frac{\partial \tilde{y}_1^*}{\partial \tilde{\Gamma}} e \tag{27}$$

and the plant output $\tilde{y}_1$ is related to the control gain $\tilde{\Gamma}$ through the plant transfer function $H(\omega_0) = \tilde{y}_1/\tilde{\Gamma}$. It follows that in this case $\partial \tilde{y}_1/\partial \tilde{\Gamma} = H$, so the update equation for a linear plant is

$$\tilde{\Gamma}(n+1,\omega_0) = \tilde{\Gamma}(n,\omega_0) - \mu H^*(\omega_0) e \tag{28}$$

which is formally identical to the update equation for a perfectly linear system.

One way of avoiding the limited performance of the feedforward control solution shown in Fig. 10 is to consider higher harmonics of the disturbance in the reference signal. The corresponding structure, shown in Fig. 11, is similar to the one proposed by others for the harmonic control of periodic disturbances of a nonlinear system [3,23]. The problem is to adjust the various complex gains $\tilde{\Gamma}_k$ that will act on each of the harmonics $k\omega_0$ in order to minimize the resulting error signal $e(t)$; the series of harmonic controllers therefore act to linearize the plant. Similar to the previous section, we have

$$y(t) = \sum_{n=0}^{N} \tilde{y}_n \exp(\mathrm{j} n \omega_0 t), \tag{29}$$

$$e(t) = \sum_{n=0}^{N} \tilde{y}_n \exp(\mathrm{j} n \omega_0 t) + \tilde{D} \exp(\mathrm{j} \omega_0 t). \tag{30}$$

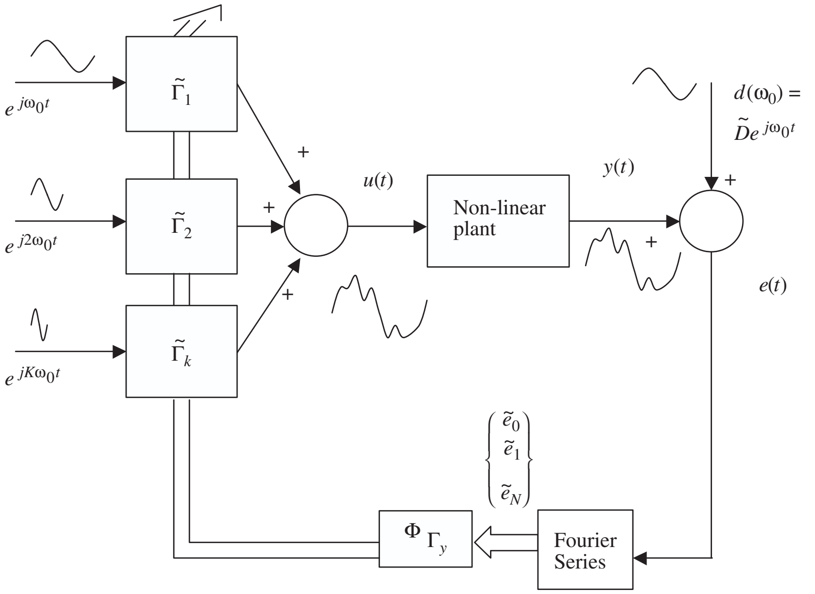

Fig. 11. Adaptation of a feedforward control of a harmonic disturbance *d* with a nonlinear plant and a multi-harmonic reference signal *x*.

The criterion is still defined as the energy of the error signal averaged over one fundamental period,

$$J = \frac{1}{T_0}\int_0^{T_0} [\mathrm{Re}(e(t))]^2\,\mathrm{d}t = \frac{1}{2}\sum_{n\neq 1} |\tilde{y}_n|^2 + \frac{1}{2}|\tilde{y}_1 + \tilde{D}|^2 = \frac{1}{2}\mathbf{e}^H\mathbf{e}, \tag{31}$$

where $\mathbf{e} = [\tilde{y}_0\, \tilde{y}_1 + \tilde{D}\, \tilde{y}_2 \ldots \tilde{y}_N]^{\mathrm{T}}$. The control acts as a series of complex gains $\tilde{\Gamma}_k$ at the various harmonics $k\omega_0$. Note again that J is not a quadratic function of the complex control gains, because there may exist a nonlinear relation between the harmonic components of the error signal and the $\tilde{\Gamma}_k$. The derivative of the criterion with respect to the control variable $\tilde{\Gamma}_k$ is

$$\frac{\partial J}{\partial \tilde{\Gamma}_k} = \frac{\partial(\frac{1}{2}\mathbf{e}^H\mathbf{e})}{\partial \tilde{\Gamma}_k} = \frac{\partial \mathbf{e}^H}{\partial \tilde{\Gamma}_k}\mathbf{e} = \frac{\partial \mathbf{y}^H}{\partial \tilde{\Gamma}_k}\mathbf{e}, \tag{32}$$

where $\mathbf{y} = [\tilde{y}_0\ \tilde{y}_1\ \tilde{y}_2 \ldots \tilde{y}_N]^{\mathrm{T}}$. Introducing the vector of complex gains $\tilde{\mathbf{\Gamma}} = [\tilde{\Gamma}_1\ \tilde{\Gamma}_2 \ldots \tilde{\Gamma}_K]$, we have

$$\frac{\partial J}{\partial \tilde{\mathbf{\Gamma}}} = \frac{\partial \mathbf{y}^H}{\partial \tilde{\mathbf{\Gamma}}}\mathbf{e} = \mathbf{\Phi}_{\mathbf{\Gamma y}}\mathbf{e}, \tag{33}$$

where $\mathbf{\Phi}_{\mathbf{\Gamma y}}$ is the sensitivity matrix of the system,

$$\mathbf{\Phi}_{\mathbf{\Gamma y}} = \begin{pmatrix} \dfrac{\partial \tilde{y}_0^*}{\partial \tilde{\Gamma}_1} & \cdots & \dfrac{\partial \tilde{y}_N^*}{\partial \tilde{\Gamma}_1} \\ \vdots & \vdots & \vdots \\ \dfrac{\partial \tilde{y}_0^*}{\partial \tilde{\Gamma}_K} & \cdots & \dfrac{\partial \tilde{y}_N^*}{\partial \tilde{\Gamma}_K} \end{pmatrix}.$$

Finally, the steepest-descent algorithm writes

$$\tilde{\mathbf{\Gamma}}(n+1) = \tilde{\mathbf{\Gamma}}(n) - \mu \mathbf{\Phi}_{\mathbf{\Gamma y}} \mathbf{e}. \tag{34}$$

In this situation, the sensitivity matrix expresses the variation of individual harmonics in the plant output with respect to individual harmonics in the signal command. The off-diagonal terms of this matrix describe the interaction between distinct harmonic frequencies which is the consequence of the plant nonlinearity. In the case of a perfectly linear plant, the sensitivity matrix is diagonal, and the control becomes as series of independent control gains at distinct harmonics ω_k. The adaptation requires an identification of the complete matrix $\hat{\mathbf{\Phi}}_{\mathbf{\Gamma y}}$ around the estimated operating point of the plant. The structure of the adaptive controller is shown in Fig. 11.

4.2. Time-domain analysis

In practice, the multi-harmonic reference signal was synthesized from a single-frequency reference signal at the fundamental frequency $\cos(\omega_0 t)$ using a "harmonic generator". Also, the series of harmonic controllers $\tilde{\Gamma}_k$ are realized via a unique finite impulse response (FIR) filter whose coefficients are noted $\mathbf{W} = [W_0 \; W_1 \ldots W_{L-1}]^{\mathrm{T}}$ (Fig. 12). The control signal is

$$u(n) = \sum_{l=0}^{L-1} W_l(n) x(n-l) = \mathbf{W}^{\mathrm{T}}(n)\mathbf{x}(n), \tag{35}$$

where $\mathbf{x}(n) = [x(n) \; x(n-1) \ldots x(n-L+1)]^{\mathrm{T}}$. The criterion is defined as the instantaneous error squared, $J = e^2(n)$. The gradient of the criterion with respect to the control filter weights is

$$\frac{\partial J}{\partial W_l} = \frac{\partial e^2(n)}{\partial W_l} = 2e(n)\frac{\partial e(n)}{\partial W_l} = 2e(n)\frac{\partial y(n)}{\partial W_l}. \tag{36}$$

At this point, it is convenient to distinguish between "static" and "dynamic" nonlinearity. In a static nonlinearity (such as a saturation) the output of the plant at time n depends only on the plant input at time n. In a dynamic nonlinearity (such as a backlash or hysteresis), the output of the plant at time n depends on the plant input at time $n, n-1, n-2, \ldots$. [3]. In the simple case of

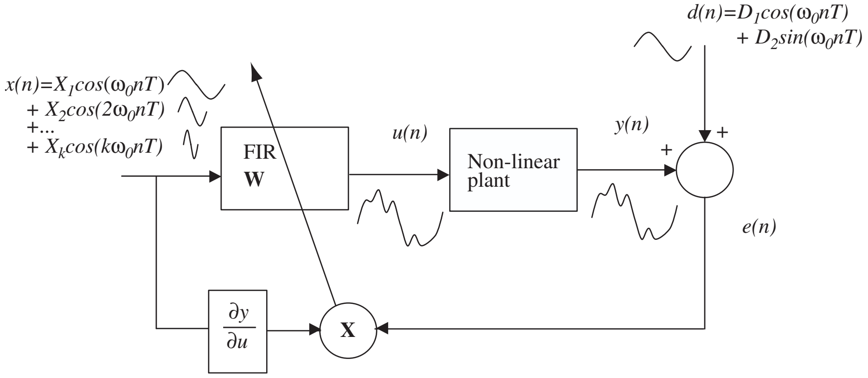

Fig. 12. Adaptation of a feedforward control of a harmonic disturbance d with a nonlinear (static) plant and a multi-harmonic reference signal x: time-domain analysis.

a static nonlinearity, we can write

$$\frac{\partial y(n)}{\partial W_l} = \frac{\partial y(n)}{\partial u(n)} \frac{\partial u(n)}{\partial W_l} = \frac{\partial y(n)}{\partial u(n)} x(n-l) \tag{37}$$

and in vector form,

$$\frac{\partial y(n)}{\partial \mathbf{W}(n)} = \frac{\partial y(n)}{\partial u(n)} \mathbf{x}(n). \tag{38}$$

Therefore, the steepest-descent algorithm takes the form

$$\mathbf{W}(n+1) = \mathbf{W}(n) - 2\mu \frac{\partial y(n)}{\partial u(n)} \mathbf{x}(n) e(n). \tag{39}$$

In contrast with a linear system, for which the gradient algorithm requires identification of the plant transfer function, the gradient algorithm for a static nonlinearity requires identification of the variation $\partial y/\partial u$ (Fig. 12). This needs to be done around the operating point of the plant. Note that this identification needs to be done for an input signal $u(n)$ that contains higher harmonics of the fundamental frequency ω_0.

4.3. Time-domain simulations

Time-domain simulations of active isolation were done based on nonlinear models of the control path H. The nonlinear model is based on the analytical Preisach model of stack actuators detailed in the Sections 2 and 3 of this paper. The disturbance frequency was fixed to 150 Hz, with an imposed displacement amplitude of 1 μm at the isolator base. The two different control algorithms that were investigated are shown in Fig. 13.

The first algorithm (A1) is a classical filtered-X LMS feedforward algorithm with a single-frequency reference. The reference signal $x(n)$ is the imposed disturbance acceleration at the isolator base. The control path H_{Pr} relates the control voltage of the stack $u(n)$ to the acceleration on top of the stack. H_{Pr} is modeled using the previous Preisach model of the stack and therefore includes hysteretic nonlinearity; for simplicity, the mass of the platform is neglected in H_{Pr} and the stack base is assumed rigid (fixed-free conditions). The control path H_{Pr} is modeled using the first of Eq. (8) in which σ_3 is set to zero; the acceleration $\ddot{\delta l}_{\mathrm{total}}$ of the stack's free end relative to the input voltage u is derived from γ_3 as a function of E_3 in the first of Eq. (8). The irreversible polarization $\hat{P}_3$ is derived from the weighting matrix $\mu(\alpha_i, \beta_j)$ in the Preisach model and the identified ferro-electro-elastic coefficients. The control filter W is a FIR filter with n_W coefficients and the model $\hat{H}$ of the secondary path H used in the adaptation of the control filter is also a linear FIR filter with $n_{\hat{H}}$ coefficients.

The second algorithm (A2) is an X-LMS feedforward with a multi-harmonic reference, similar to Fig. 12. In this case, the single-frequency reference signal is passed through a harmonic generator in order to synthesize higher harmonics of the disturbance before multiplication by the FIR control filter. This harmonic generator was taken to be the nonlinear plant model H_{Pr} introduced in the first section of this paper. Although the reference is a single-frequency signal in this case, the control signal contains the harmonics of the disturbance necessary to compensate the stack nonlinearity. Also, the adaptation uses a *linear* model of the variation $\partial y/\partial u$ in Fig. 12. This

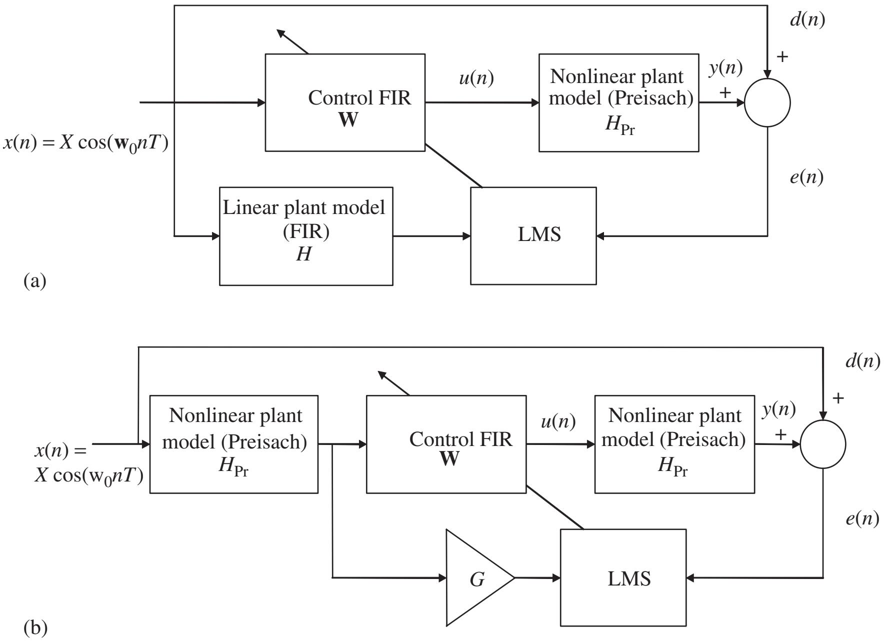

Fig. 13. Active control algorithms investigated in time-domain simulations (a) single-frequency reference and (b) multiple-frequencies reference.

linear model was simply taken to be a real gain G between the input voltage of the stack and the acceleration on top of the stack, derived from the *linear* constitutive equations of the stack equations (11).

Note that in Fig. 13, the disturbance acceleration transmitted to the platform when $u = 0$ is equal to the base acceleration since the actuator is assumed perfectly rigid. In all cases, the error signal e is the transverse acceleration transmitted to the platform, and the criterion minimized by the control filter is the instantaneous acceleration squared e^2. The parameters chosen in the time-domain simulations were $n_W = 128$ coefficients for the control FIR filter, $n_{\hat{H}} = 100$ coefficients for the identification filter and the sampling frequency was set to 2.5 kHz.

Fig. 14 shows simulation results for algorithms A1 and A2 in terms of the FFT of the error signal before control and after convergence of the 2 control algorithms. Table 1 summarizes transmitted acceleration levels at the disturbance frequency and at the first and second harmonics of the disturbance after control, as well as the attenuation obtained at the disturbance frequency with respect to the control off case. As expected, the controller with a single-frequency reference (A1, Fig. 14(a)) is effective in cancelling the disturbance frequency at 150 Hz, but the actuator nonlinearity produces harmonic generation at the first harmonic (300 Hz) and especially at the second harmonic (450 Hz). In this case, the transmitted acceleration levels at the disturbance frequency and the first and second harmonics are $-63.7, -56.7$ and -45.6 dB, respectively; the attenuation of the disturbance frequency is 25 dB. The control filter weights for the various algorithms, as well as their FFT are plotted in Fig. 15. In the case of A1 (Fig. 15(a)) the filter weights have a sinusoidal variation at the disturbance frequency, which shows that the control

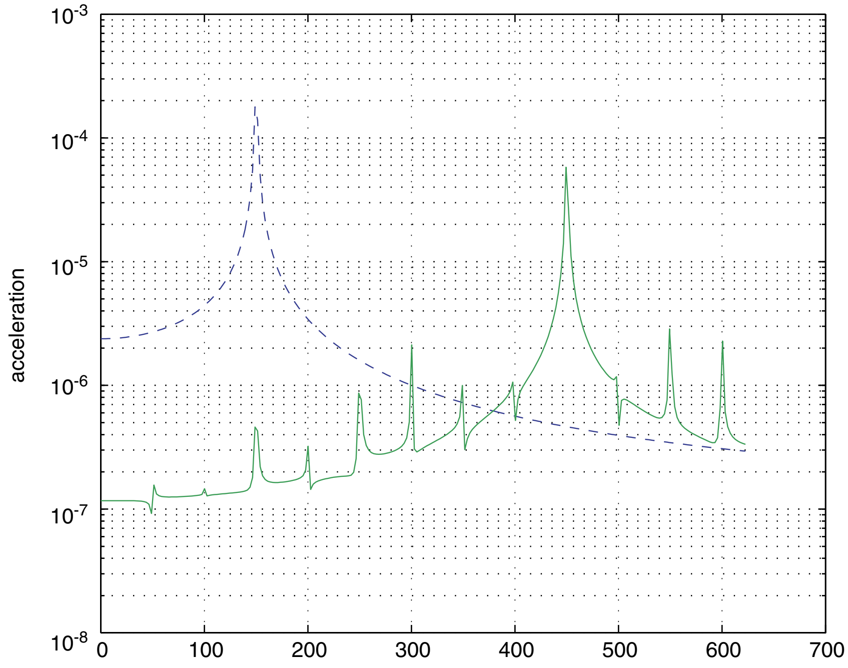

(a)

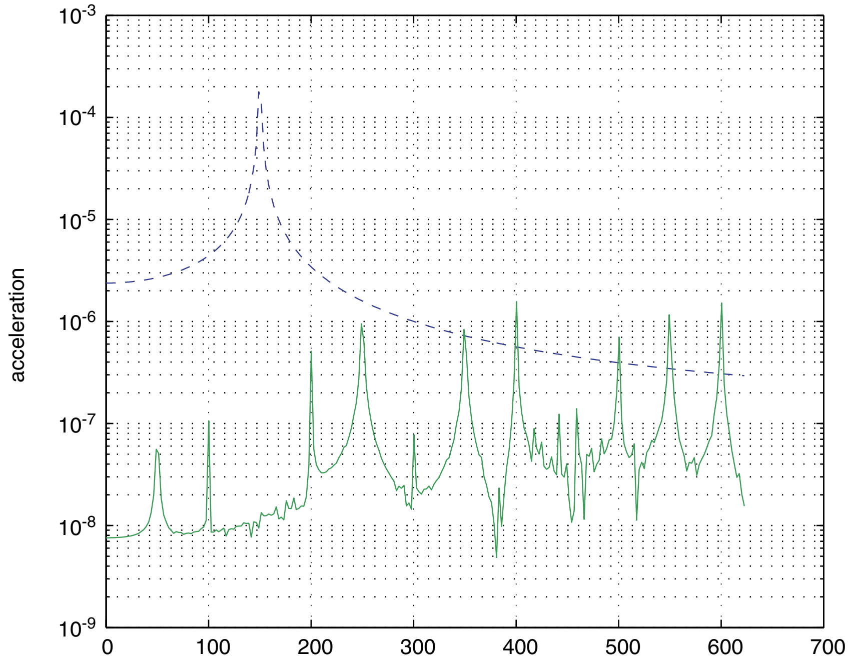

(b)

Fig. 14. Results of time-domain control simulations: FFT of error signal with control on (solid line)/off (dashed line). (a) single-frequency reference and (b) multiple-frequency reference.

Table 1
Active control simulations: results at disturbance frequency and first two harmonics

Algorithm	Attenuation at disturbance frequency (dB)	Acceleration level at disturbance frequency (dB)	Acceleration level at first harmonic (dB)	Acceleration level at second harmonic (dB)
A1	25	−63.7	−56.7	−45.6
A2	40.6	−78.7	−71.1	−77.5

signal is also perfectly sinusoidal at the disturbance frequency: the actuator nonlinearity cannot be compensated in this case. In Fig. 14(a), the additional peaks at multiples of 50 Hz are due to numerical errors in the estimation of accelerations from actuator deformation using sampled data.

The use of the multiple-frequency reference significantly improves the control effectiveness at higher harmonics of the disturbance (algorithm A2, Fig. 14(b)), even though the plant model in the adaptation is linear. In this case, the transmitted acceleration levels at the disturbance frequency and the first and second harmonics are $-78.7, -71.1$ and -77.5 dB, respectively; the attenuation of the disturbance frequency is 40.6 dB and the first and second harmonics are decreased by 14.4 and 32 dB, respectively, with respect to algorithm A1. The weights of the FIR control filter (Fig. 15(b)) show that the control signal is a multi-harmonic signal that contains higher harmonics of the disturbance frequency in this case (despite the fact that the reference is a single-frequency signal). The control algorithm adequately compensates the actuator nonlinearity.

5. Active vibration isolation using a piezoelectric stack actuator: Experiments

An active isolator using a piezoceramic stack actuator was built (Fig. 9). The actuator is the same BM532 PZT5H Sensor Technology stack as presented in the modeling section; the stack measures approximately 2 cm in height and 1 cm × 1 cm in cross-section. The actuator was encased under compressive preloading in an aluminum cylinder in order to ensure operation under dynamic compressive loads. The suspended platform is a rigid aluminum block which is attached to the top end of the stack. Its mass is about 29 g with the error accelerometer. Small elastomer mounts are also used between the casing and the top mass. The error sensor is an Oceana Sensor Technologies ICP accelerometer ($1000\,\mathrm{mV}/G$). The isolator was mounted on a flexible plate and the disturbance was generated by an electrodynamic shaker exciting the base plate at a frequency of 150 Hz. Fig. 16 shows the resulting acceleration measured by the error sensor on the suspended mass. The acceleration on top of the isolator contains significant components at the first and second harmonics of the disturbance frequency (the level of the second harmonic is about 15 dB below the disturbance frequency): the isolator in its passive form has therefore some inherent nonlinearity, which is due to mechanical looseness in the mounting of the piezo stack in the isolator casing. Therefore, in contrast with the previous simulations, not only the control path but also the primary path has some nonlinear behavior in the experiments. Two active control algorithms A1e, A2e essentially similar to A1 and A2 were experimentally implemented in the DSpace environment for real time control.

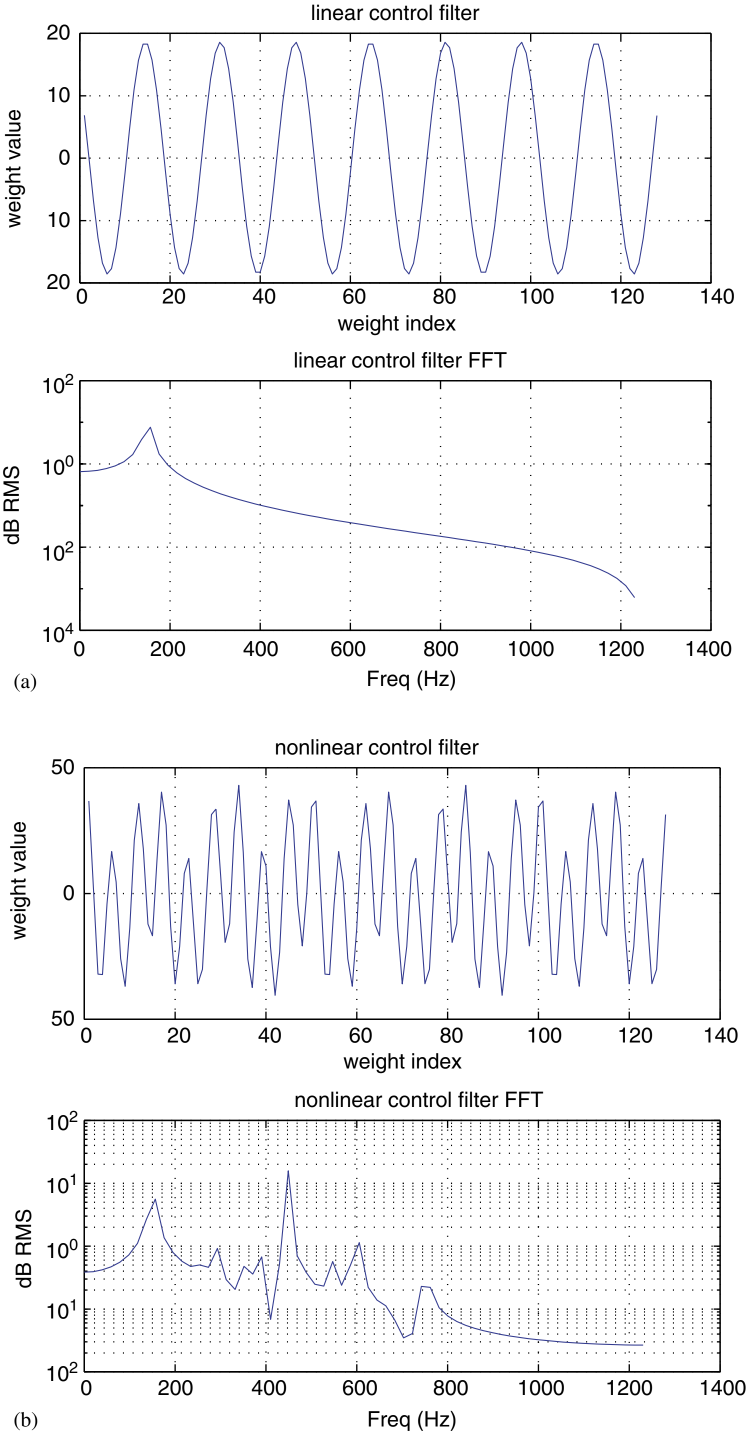

Fig. 15. Control filter weights: (a) single-frequency reference and (b) multiple-frequency reference.

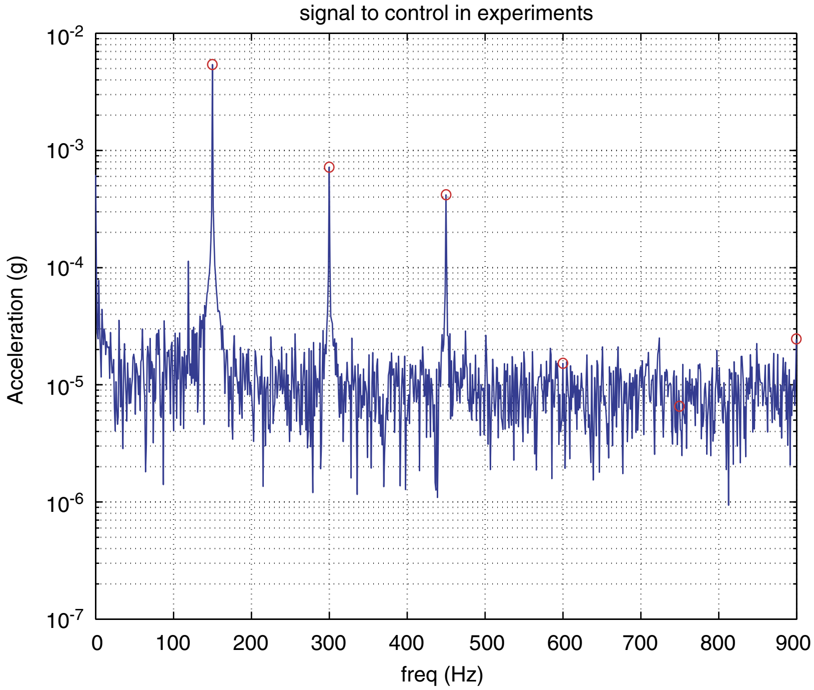

Fig. 16. FFT of acceleration at error sensor due to the primary disturbance.

The first algorithm (A1e) is a filtered-X LMS feedforward algorithm with a single-frequency reference. The reference signal x is the input signal to the disturbance shaker. The control filter W is a linear FIR filter with n_W coefficients and the model $\hat{H}$ of the secondary path H used in the adaptation of the control filter is also a linear FIR filter with $n_{\hat{H}}$ coefficients.

The second algorithm (A2e) is a filtered-X LMS feedforward algorithm with a multiple-frequency reference. The reference signal was synthesized by passing the single-frequency disturbance x through the nonlinear model of the plant H_{Pr}, as shown in Fig. 13. Also, the adaptation uses a linear model of the variation $\partial y/\partial u$ in Fig. 12. This linear model is a real gain G derived from the linear constitutive equations of the stack equations (11).

The control parameters chosen in the experiments are the same as in the simulations: $n_W = 128$, $n_{\hat{H}} = 100$ and the sampling frequency was 2.5 kHz.

Fig. 17 shows the experimental results in terms of the FFT of the error before and after control using the 2 control algorithms. A1e allows rejection of the disturbance frequency only, since only the disturbance frequency is observed in the reference signal. The attenuation of the disturbance frequency, 1st (300 Hz), 2nd (450 Hz) and 3rd (600 Hz) harmonics are 33.7, –0.2, 1.3 and –4.3 dB, respectively (a negative value meaning an increase).

A significantly better control performance is obtained with the algorithm A2e that includes the nonlinear model of the control path as harmonics generator, and a linear gain in the adaptation path: in this case, both the disturbance frequency and the first 3 harmonics are significantly reduced. The attenuation of the disturbance frequency, 1st, 2nd and 3rd harmonics are 31.3, 9.4, 15.6 and 6.7 dB, respectively. These observations confirm the results of the control simulations.

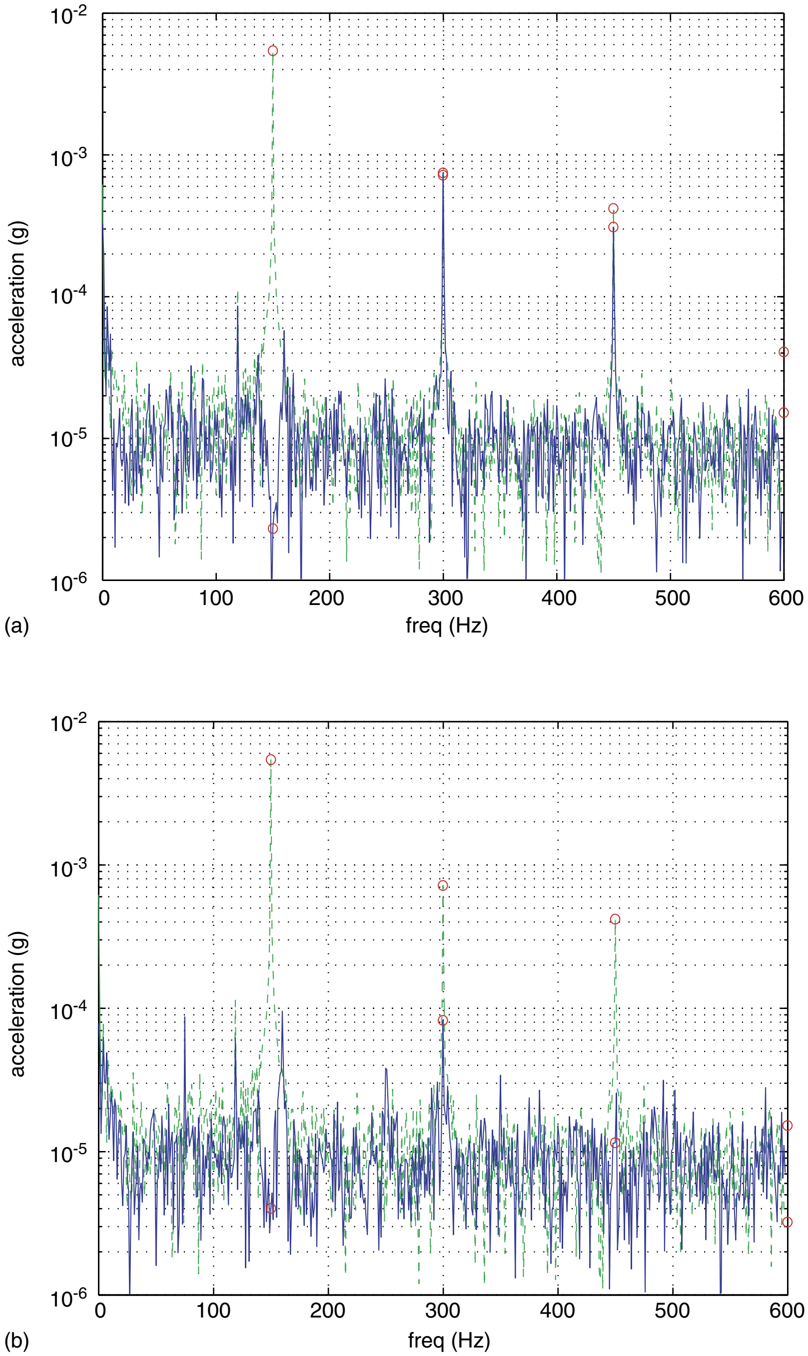

Fig. 17. Experimental control results: FFT of error signal with control on (solid line)/off (dashed line): (a) linear algorithm and (b) nonlinear algorithm.

6. Conclusions

An analytical model of a piezoelectric stack actuator including hysteresis has been presented. Compared to the constitutive equations of linear piezoelectricity, the nonlinear model involves new ferro-electro-elastic constants that account for hysteretic behavior between applied electric field and resulting polarization. The minor hysteresis loops of the actuator have been identified with a Preisach model, which allows the new constants to be identified through simultaneous measurement of applied voltage, polarization and displacement. In the context of active isolation of single-frequency disturbance using a piezoelectric stack actuator, the hysteretic response of the actuator generates higher harmonics of the disturbance in the error signal. It was shown that pre-multiplication of a single-frequency reference by a higher harmonic generator effectively compensates the actuator nonlinearity. The nonlinear model of the stack was implemented in real-time as harmonic generator in a X-LMS feedforward controller for active vibration isolation of single-frequency disturbance. Both simulation and experimental results show that both the disturbance frequency and its first higher harmonics can be effectively controlled.

References

[1] C.G. Gordon, Vibration control in microelectronics, optics, and metrology, *Proceedings, SPIE—The International Society for Optical Engineering*, San Jose, California, 1619 (also published by Society of Photo Optical, October 1992, ISBN 0819407577).

[2] J. Cruz-Hernàndez, V. Hayward, An approach to reduction of hysteresis in smart materials, in: *Proceedings of the IEEE International Conference on Robotics and Automation*, Leuven, Belgium, 1998, pp. 1510–1515.

[3] S. Elliot, *Signal Processing for Active Control*, first ed., Academic Press, New York, 2001.

[4] H. Hu, R. Mrad, Limitations of the classical Preisach model for hysteresis in piezoceramics actuators, in: *Proceedings of the Third Cansmart Workshop on Smart Materials and Structures*, 2000, pp. 125–131.

[5] H. Hu, R. Mrad, Preisach modeling of hysteresis in a piezoceramic actuator, *Smart Materials and Structures Second CanSmart Workshop 1999*, 1999, pp. 31–40.

[6] R.B. Mrad, H. Hu, A model for voltage-to-displacement dynamics in piezoceramic actuators subject to dynamic voltage excitations, *IEEE/ASME Transactions on Mechatronics* 7 (2002) 479–489.

[7] R.B. Mrad, Nonlinear systems representation using armax models with time dependent coefficients, *Mechanical Systems and Signal Processing* 16 (2001) 803–815.

[8] K. Kuhnen, H. Janocha, Adaptive inverse control of piezoelectric actuators with hysteresis operators, *European Control Conference ECC1999*, 1999, F291.

[9] P. Krejci, K. Kuhnen, Inverse control of systems with hysteresis and creep, *IEEE Proceedings: Control Theory and Applications* 148 (2001) 185–192.

[10] K. Kuhnen, H. Janocha, Inverse feedforward controller for complex hysteretic nonlinearities in smart-material systems, *Control and Intelligent Systems* 29 (2001) 55–63.

[11] K. Kuhnen, H. Janocha, A dynamic vibration absorber based on smart piezoelectric actuators, in: *Mechatronics 2002*, *Proceedings of the Eighth Mechatronics Forum International Conference*, 2002, pp. 1048–1057.

[12] H. Tiersten, *Linear Piezoelectric Plate Vibrations: Elements of the Linear Theory of Piezoelectricity and the Vibrations of Piezoelectric Plates*, Plenum Press, New York, 1969.

[13] H.F. Tiersten, Electroelastic equations for electrode thin plates subject to large driving voltages, *Journal of Applied Physics* 74 (1993) 3389–3393.

[14] J.S. Yang, R.C. Batra, Mixed variational principles in nonlinear electroelasticity, *International Journal of Nonlinear Mechanics* 30 (5) (1995) 719–725.

[15] L. Huang, H. Tiersten, Electroelastic equations describing slow hysteresis in polarized ferroelectric ceramic plates, *Journal of Applied Physics* 83 (11) (1998) 6126–6139.

[16] Y. Pasco, A. Berry, A hybrid analytical/numerical model of piezoelectric stack actuators using a macroscopic nonlinear theory of ferroelectricity and a Preisach model of hysteresis, *Journal of Intelligent Materials, Systems and Structures* 15 (5) (2004) 375.

[17] Y. Pasco, Étude Physique d'un Actionneur Piézoélectrique Multi-couches Non-linéaire et Applications á l'Absorption Active des Vibrations Déterministes sur 1 puis 6 Degrés de Liberté, PhD Thesis, University of Sherbrooke, 2002.

[18] I. Mayergoyz, *Mathematical Models of Hysteresis*, Springer, Berlin, 1991.

[19] P.T.J.J. Rousseau, L. Zegadi, Amélioration du modèle de preisach. Application aux matériaux magnétiques doux, *Journal de Physique III* (8) (1997) 1717–1727.

[20] E.D. Torre, Hysteresis modeling, *COMPEL—The International Journal for Computation and Mathematics in Electrical and Electronic Engineering* 17 (5/6) (1998) 682–689.

[21] K. Levenberg, A method for the solution of certain problems in least squares, *Quarterly of Applied Mathematics* 2 (1944) 164–168.

[22] D. Marquardt, An algorithm for least-squares estimation on nonlinear parameters, *SIAM Journal on Applied Mathematics* 11 (1963) 431–441.

[23] T. Sutton, S. Elliott, Active attenuation of periodic vibration in nonlinear systems using an adaptive harmonic controller, *Journal of Vibration and Acoustics* 117 (1995) 355–362.